

Atomic transport properties of liquid iron at conditions of planetary cores

Cite as: J. Chem. Phys. **155**, 194505 (2021); <https://doi.org/10.1063/5.0062081>

Submitted: 02 July 2021 • Accepted: 31 October 2021 • Accepted Manuscript Online: 01 November 2021 • Published Online: 18 November 2021

 Qing Li,  Tao Sun,  Yi-gang Zhang, et al.



View Online



Export Citation



CrossMark

ARTICLES YOU MAY BE INTERESTED IN

[Molecular dynamics simulation of metallic Al-Ce liquids using a neural network machine learning interatomic potential](#)

The Journal of Chemical Physics **155**, 194503 (2021); <https://doi.org/10.1063/5.0066061>

[Static and dynamic water structures at interfaces: A case study with focus on Pt\(111\)](#)

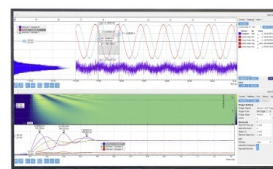
The Journal of Chemical Physics **155**, 194702 (2021); <https://doi.org/10.1063/5.0067106>

[Probing the theoretical and computational limits of dissipative design](#)

The Journal of Chemical Physics **155**, 194114 (2021); <https://doi.org/10.1063/5.0067695>

Challenge us.

What are your needs for
periodic signal detection?



Zurich
Instruments

Atomic transport properties of liquid iron at conditions of planetary cores

Cite as: J. Chem. Phys. 155, 194505 (2021); doi: 10.1063/5.0062081

Submitted: 2 July 2021 • Accepted: 31 October 2021 •

Published Online: 18 November 2021



View Online



Export Citation



CrossMark

Qing Li,¹ Tao Sun,^{1,a)} Yi-gang Zhang,¹ Jia-Wei Xian,² and Lidunka Vočadlo³

AFFILIATIONS

¹Key Laboratory of Computational Geodynamics, College of Earth and Planetary Sciences, University of Chinese Academy of Sciences, Beijing 100049, China

²Laboratory of Computational Physics, Institute of Applied Physics and Computational Mathematics, Beijing 100088, China

³Department of Earth Sciences, University College London, Gower Street, London WC1E 6BT, United Kingdom

^{a)}Author to whom correspondence should be addressed: tsun@ucas.ac.cn

ABSTRACT

Atomic transport properties of liquid iron are important for understanding the core dynamics and magnetic field generation of terrestrial planets. Depending on the sizes of planets and their thermal histories, planetary cores may be subject to quite different pressures (P) and temperatures (T). However, previous studies on the topic mainly focus on the P - T range associated with the Earth's outer core; a systematic study covering conditions from small planets to massive exoplanets is lacking. Here, we calculate the self-diffusion coefficient (D) and viscosity (η) of liquid iron via *ab initio* molecular dynamics from 7.0 to 25 g/cm³ and 1800 to 25 000 K. We find that D and η are intimately related and can be fitted together using a generalized free volume model. The resulting expressions are simpler than those from previous studies where D and η were treated separately. Moreover, the new expressions are in accordance with the quasi-universal atomic excess entropy (S_{ex}) scaling law for strongly coupled liquids, with normalized diffusivity $D^* = 0.621 \exp(0.842S_{\text{ex}})$ and viscosity $\eta^* = 0.171 \exp(-0.843S_{\text{ex}})$. We determine D and η along two thermal profiles of great geophysical importance: the iron melting curve and the isentropic line anchored at the ambient melting point. The variations of D and η along these thermal profiles can be explained by the atomic excess entropy scaling law, demonstrating the dynamic invariance of the system under uniform time and space rescaling. Accordingly, scale invariance may serve as an underlying mechanism to unify planetary dynamos of different sizes.

Published under an exclusive license by AIP Publishing. <https://doi.org/10.1063/5.0062081>

I. INTRODUCTION

Terrestrial planets often possess iron-dominant cores that are partially or completely molten.¹⁻⁴ Dynamic behavior of its liquid core plays a prominent role in shaping the planet's overall features. For instance, the rapid fluidic motion inside the liquid core is believed to be responsible for the planet's magnetic field.⁵⁻⁷ The viscous friction between the liquid core and the solid mantle is one of the main mechanisms for core-mantle coupling.⁸ Moreover, the gradual cooling of the liquid core provides the ultimate energy source driving the movements of the mantle and crust.⁹ To better understand the dynamics and thermal evolution of the liquid core, precise knowledge on its transport properties is essential. Here, we focus on atomic transport properties, namely, the self-diffusivity (D) and viscosity (η). These properties have been investigated before,¹⁰⁻¹⁵ however, they are mostly conducted under

the pressure (P) and temperature (T) conditions of the Earth's outer core (136–330 GPa, 4000–6000 K). With increased interest in planets such as Mars² and Mercury⁴ where the core pressures are tens of GPa, as well as the discovery of exoplanets where the core pressures may exceed 2 TPa,¹⁶ it would be desirable to expand the investigation to a greater range, so as to determine how the dynamic behavior of the core may be affected by the varying P - T conditions.

At first sight, one may not expect that the dynamic behavior of a system at one P - T condition can be intimately related to that of another. Yet a connection has been discovered by Rosenfeld in the form of the atomic excess entropy scaling law.^{17,18} According to this law, a system will exhibit identical (up to a uniform time and space rescaling) dynamic behavior at different P - T conditions, insofar as they share the same atomic excess entropy (S_{ex}). As such, both D and η can be normalized and expressed as functions of S_{ex} only. The

atomic excess entropy scaling law has been validated successfully in many systems.¹⁹ Cao *et al.*²⁰ examined the atomic excess entropy scaling law for liquid iron using classical molecular dynamics (MD) at the P - T conditions of the Earth's outer core. The normalized diffusivity and viscosity were found to be $D^* = 0.383 \exp(0.707S_{\text{ex}})$ and $\eta^* = 0.412 \exp(-0.688S_{\text{ex}})$, respectively. These results are promising, yet further consideration may be still needed: iron is a metal. Its electronic thermal excitations are significant under the P - T conditions of planetary cores. Unfortunately, such excitations are absent in classical MD, leading to substantially lower total entropies than those predicted from *ab initio* simulations.²¹ Moreover, the atomic excess entropy used in the work was not the exact S_{ex} , but a two-body approximation (S_2) derived from pair distribution functions. As the difference between S_2 and S_{ex} can reach 15% or more,²² it remains to be seen how the transport properties of liquid iron scale with respect to the exact S_{ex} .

Here, we run *ab initio* MD (AIMD) to calculate D and η of liquid iron from 7.0 to 25 g/cm³, with T ranging from 1800 to 25 000 K. The substantially wider range allows us to identify the density and temperature dependences of transport properties more clearly. We use a recently developed *ab initio* thermodynamic integration (TI) scheme to determine the absolute entropy of the system, from which we extract the exact S_{ex} and verify the atomic excess entropy scaling law. We further determine D and η along two temperature profiles of great geophysical significance: the iron melting curve and the isentropic line anchored at the ambient melting point (0 GPa, 1811 K). The atomic excess entropy scaling law is then applied to explain the observed pressure dependence.

II. METHODS

We ran AIMD simulations in the projected-augmented-wave (PAW) formalism^{23,24} using the Vienna *Ab initio* Simulation Package (VASP).^{25,26} The generalized-gradient approximation (GGA) parameterized by Perdew, Burke, and Ernzerhof (PBE)²⁷ was chosen to describe the electron-electron exchange-correlation interaction. The PAW pseudopotential ("Fe_sv") contains 16 valence electrons ($3s^2 3p^6 3d^7 4s^1$), as previous studies^{21,28} have shown that including the $3s$ and $3p$ electrons as valence is crucial to get accurate physical properties of liquid iron in the high P - T regime. Although this pseudo-potential has a core radius (1.9 a.u.) 15% greater than one-half of the mean interatomic distance at 25 g/cm³, the predictions it makes agree well with those from all-electron calculations²⁹ and two PAW pseudo-potentials with 16 valence electrons and smaller core-radii (1.6 a.u.³⁰ for VASP and 1.5 a.u. for Quantum Espresso³¹). We therefore conclude that the difference in the core-radii is inconsequential among these Fe pseudo-potentials with 16 valence electrons and "Fe_sv" is appropriate for our purpose (see the [supplementary material](#) for details). The kinetic energy cutoff for the plane wave expansion was set to be 650 eV, and the Brillouin zone sampling was limited to the Γ -point. As such, the energy and stress were converged to 3.4 meV/atom and 1.4 GPa at 7.0 g/cm³ and 6.0 meV/atom and 5.8 GPa at 25 g/cm³; the mean errors in ionic forces were 0.01 eV/Å at 7.0 g/cm³ and 0.1 eV/Å at 25 g/cm³, respectively. Errors of such magnitude are typical among AIMD simulations³² and are adequate for the present study. The cubic simulation cell contained 108 iron atoms, with the ionic temperature controlled by using a

Nosé thermostat.³³ The electronic thermal excitations were treated by minimizing the Mermin functional.³⁴ Each simulation first ran 0.5–1 ps for thermal equilibration and then another 10 ps for production (see the [supplementary material](#) for convergence tests). The time step was set to be 1 fs, which corresponds to 1/15 of the shortest vibrational period³⁵ at the highest density (25 g/cm³). A shorter time step (0.5 fs) was found to have little influence on the final results.

To overcome the uncertainties associated with GGA, we introduce a temperature-independent pressure correction³⁶ in the form of a sigmoid function as

$$\Delta P(\rho_m) = \frac{17.38}{1 + \exp((\rho_m - 11.395) \cdot 1.341)}, \quad (1)$$

where the unit of ΔP is GPa and the unit of ρ_m is g/cm³. This correction is significant at low densities (about 17 GPa between 7.0 and 9.0 g/cm³) yet becomes less than 1 GPa beyond 13.5 g/cm³. The resulting thermal equation of state $P(\rho_m, T)$ is in excellent agreement with experiments.³⁷

The self-diffusion coefficient of a liquid can be evaluated via two methods: One is from the long time slope of the mean square displacement (MSD),³⁸

$$D = \lim_{t \rightarrow \infty} \frac{1}{N} \sum_{i=1}^N \frac{\langle |\mathbf{r}_i(t) - \mathbf{r}_i(0)|^2 \rangle}{6t}, \quad (2)$$

where N is the total number of atoms, $\mathbf{r}_i(t)$ represents the trajectory of the i th iron atom at time t , and $\langle \dots \rangle$ stands for the ensemble average. The error in the diffusivity is estimated by evaluating the standard deviation of the long time slopes of the MSD among individual atoms and then dividing it by \sqrt{N} . Alternatively, D is determined through the power spectrum (vibrational density of states, VDoS) of the velocity autocorrelation function (VACF). The VACF $C_{vv}(t)$ and its power spectrum $F(v)$ are defined as^{35,39}

$$C_{vv}(t) = \frac{1}{3(N-1)} \sum_{i=1}^N m \langle \mathbf{v}_i(0) \cdot \mathbf{v}_i(t) \rangle, \quad (3)$$

$$F(v) = \frac{12}{k_B T} \int_0^\infty C_{vv}(t) \cos(2\pi vt) dt, \quad (4)$$

where m is the mass of the atom, $\mathbf{v}_i(t)$ denotes the velocity of the i th atom at time t , k_B is the Boltzmann constant, and T is the temperature. The diffusivity D is proportional to the VDoS at zero frequency $F(0)$ as^{40,41}

$$D = \frac{k_B T}{12m} F(0). \quad (5)$$

The viscosity of a liquid is determined from the linear-response Green-Kubo formula as

$$\eta = \int_0^\infty C_{\sigma\sigma}(t) dt,$$

with $C_{\sigma\sigma}(t)$ being the stress autocorrelation function (SACF). For an isotropic system, $C_{\sigma\sigma}(t)$ can be evaluated via

$$C_{\sigma\sigma}(t) = \frac{V}{5k_B T} \sum_{s=1}^5 \langle \sigma_s(0) \sigma_s(t) \rangle, \quad (6)$$

where V is the volume of the system and σ_s represents the five independent components of the shear stress tensor: σ_{xy} , σ_{yz} , σ_{zx} , and $\frac{1}{2}(\sigma_{xx} - \sigma_{yy})$, and $\frac{1}{2}(\sigma_{yy} - \sigma_{zz})$.¹⁰ The error in the viscosity is estimated by evaluating the standard deviation of the time integral of the SACF among different stress components and then dividing the standard deviation by $\sqrt{5}$. Besides the formally exact linear-response approach, the viscosity of liquid iron has also been determined approximately from diffusivity using the Stokes–Einstein relation.⁴² However, this relation may break down,⁴³ even for a simple liquid such as Al.⁴⁴ It is therefore preferable to first evaluate the viscosity and diffusivity as independent quantities and then verify whether they satisfy the Stokes–Einstein relation. This is the approach we take in the present study.

III. RESULTS

A. MSD, VDoS, and SACF

The fundamental quantities for evaluating the diffusivity are the MSD and the VDoS. Figure 1 shows the MSDs and the VDoS at representative temperatures and densities. The linear increase in MSDs with time and the non-zero $F(0)$ of VDoS indicate that the system is in the fluid state. Moreover, the self-diffusivities determined from the long time slope of MSD and $F(0)$ differ by less than 5%, validating both approaches.

The basic quantity for determining shear viscosity is the SACF $C_{\sigma\sigma}(t)$. As shown in Fig. 2, $C_{\sigma\sigma}(t)$ decays rapidly when t is small. It decays more slowly when t grows larger, making direct numerical integration $\int_0^\infty C_{\sigma\sigma}(t)dt$ hard to converge. To overcome this

problem, we first fit $C_{\sigma\sigma}(t)$ with the following function:

$$C_{\sigma\sigma}(t) = G_\infty \left[(1 - \alpha) \operatorname{sech}^2(t/\tau_1) + \alpha e^{-t/\tau_2} \right], \quad (7)$$

where τ_1 and τ_2 are relaxation times, α is the partition factor, and G_∞ is related to $C_{\sigma\sigma}(t)$ as $G_\infty \equiv C_{\sigma\sigma}(0)$. The shear viscosity η can then be determined analytically as

$$\eta = G_\infty [(1 - \alpha)\tau_1 + \alpha\tau_2]. \quad (8)$$

Compared to direct numerical integration, this analytic integration approach⁴⁵ is less sensitive to the statistical noise whose magnitude is comparable to or even greater than $C_{\sigma\sigma}(t)$ at large t , leading to more accurate η .

B. Transport properties

Figure 3 shows the discrete D and η results from AIMD. The numerical values are listed in Table I. Our aim is to construct a suitable model from these data so as to get D and η for arbitrary density and temperature. A model frequently employed in prior studies^{15,20} is the Arrhenius model,

$$D_{\text{Arrh}}(V, T) = D_0 \exp[Q_D(V, T)], \quad (9)$$

$$\eta_{\text{Arrh}}(V, T) = \eta_0 \exp[Q_\eta(V, T)], \quad (10)$$

where D_0 and η_0 are pre-exponential constants, Q_D and Q_η are activation energies normalized to the thermal energy $k_B T$. The Arrhenius model is closely related to the transition state theory of

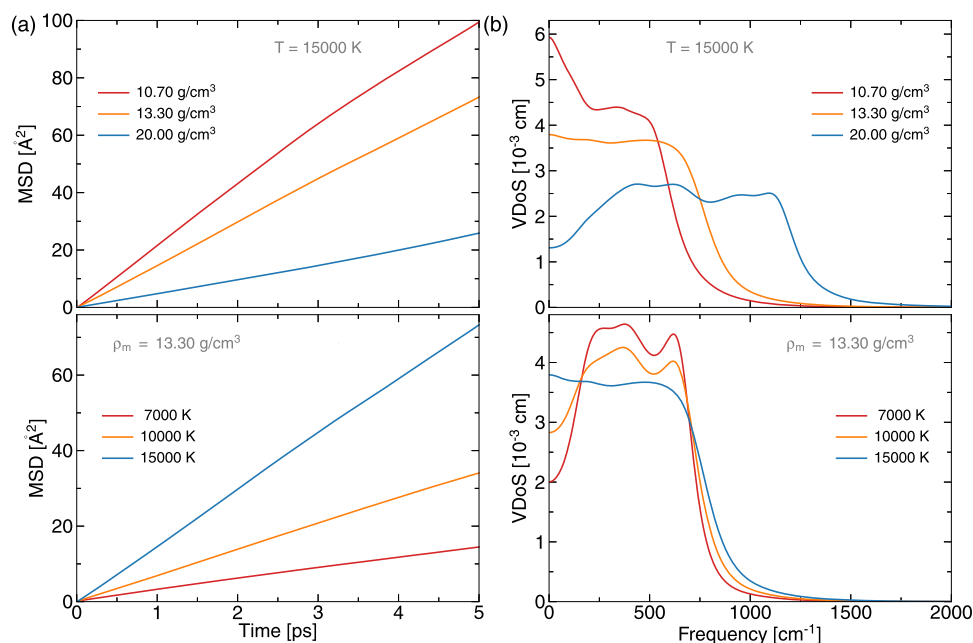


FIG. 1. (a) Mean square displacements (MSDs) and (b) vibrational density of states (VDoS) of liquid iron at representative densities and temperatures.

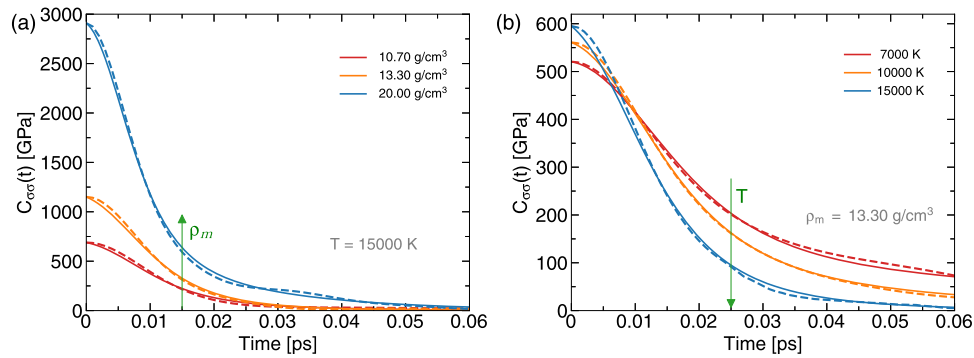


FIG. 2. Stress autocorrelation functions (SACFs) of liquid iron at representative (a) densities and (b) temperatures. The solid lines denote AIMD results, and the dashed lines are the numerical fits using Eq. (7).

statistical mechanics and is widely used in describing atomic diffusion of solids. However, there is little theoretical justification to apply it to liquids where the local environment is constantly fluctuating.⁴⁶ An alternative model describing the diffusivity of liquids is the free volume model (FVM),⁵⁰

$$D_{\text{FVM}}(V, T) = \rho^{-1/3} \sqrt{k_B T / m C_D} \exp [v_D(V, T)], \quad (11)$$

where $\rho \equiv N/V$ is the number density, m is the mass of the atom, C_D is a constant, and v_D is the normalized activation volume for diffusivity. The key difference between the Arrhenius model and the free volume model lies in their pre-exponential factors: the pre-exponential factor in the Arrhenius model is a constant D_0 with the dimension of diffusivity, whereas the pre-exponential factor in the free volume model is a dimensionless constant C_D

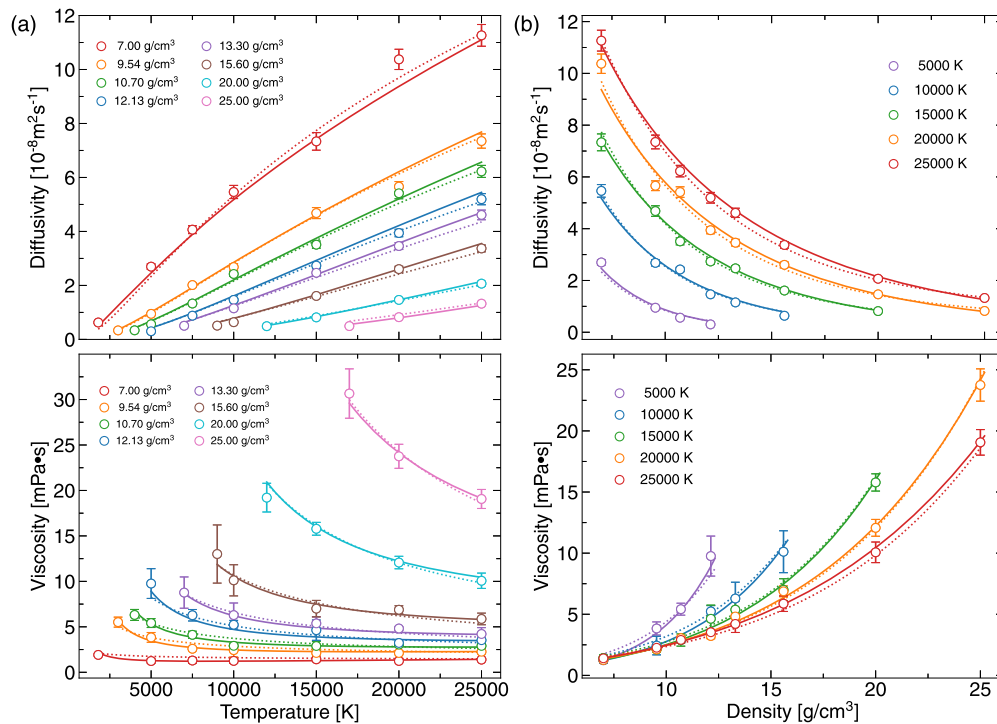


FIG. 3. Diffusivity and viscosity of liquid iron as a function of (a) temperature and (b) density. The open circles represent the calculated results, and the solid (dotted) lines denote fittings according to the extended free volume model (Arrhenius model).

TABLE I. Diffusivity (D) and viscosity (η) of liquid iron from non-spin-polarized AIMD simulations.

ρ (g/cm ³)	T (K)	D (10 ⁻⁸ m ² /s)	η (mPa s)	ρ (g/cm ³)	T (K)	D (10 ⁻⁸ m ² /s)	η (mPa s)
7.0	1 800	0.63(0.04)	1.92(0.16)	12.13	7 500	0.88(0.03)	6.27(0.63)
7.0	5 000	2.70(0.10)	1.24(0.23)	12.13	10 000	1.46(0.06)	5.23(0.48)
7.0	7 500	4.07(0.15)	1.29(0.30)	12.13	15 000	2.73(0.10)	4.63(1.12)
7.0	10 000	5.46(0.24)	1.26(0.27)	12.13	20 000	3.94(0.14)	3.22(0.22)
7.0	15 000	7.34(0.33)	1.43(0.25)	12.13	25 000	5.20(0.21)	3.53(0.13)
7.0	20 000	10.37(0.38)	1.25(0.05)	13.3	7 000	0.51(0.02)	8.77(1.72)
7.0	25 000	11.26(0.40)	1.40(0.08)	13.3	10 000	1.15(0.05)	6.29(1.33)
9.54	3 000	0.33(0.01)	5.52(0.55)	13.3	15 000	2.47(0.10)	5.38(0.71)
9.54	5 000	0.95(0.04)	3.84(0.54)	13.3	20 000	3.46(0.13)	4.82(0.19)
9.54	7 500	2.01(0.08)	2.59(0.21)	13.3	25 000	4.61(0.18)	4.21(0.70)
9.54	10 000	2.68(0.12)	2.44(0.76)	15.6	9 000	0.51(0.01)	13.01(3.20)
9.54	15 000	4.68(0.21)	2.12(0.20)	15.6	10 000	0.64(0.02)	10.12(1.71)
9.54	20 000	5.66(0.19)	2.12(0.07)	15.6	15 000	1.61(0.07)	7.00(0.90)
9.54	25 000	7.35(0.27)	2.26(0.22)	15.6	20 000	2.60(0.11)	6.88(0.44)
10.7	4 000	0.34(0.01)	6.31(0.60)	15.6	25 000	3.37(0.13)	5.87(0.64)
10.7	5 000	0.56(0.02)	5.42(0.49)	20	12 000	0.49(0.02)	19.21(1.58)
10.7	7 500	1.33(0.05)	4.12(0.40)	20	15 000	0.82(0.04)	15.78(0.71)
10.7	10 000	2.43(0.08)	2.91(0.19)	20	20 000	1.46(0.06)	12.07(0.69)
10.7	15 000	3.51(0.13)	2.89(0.50)	20	25 000	2.07(0.09)	10.07(0.84)
10.7	20 000	5.42(0.20)	3.05(0.11)	25	17 000	0.49(0.02)	30.66(2.72)
10.7	25 000	6.22(0.22)	2.90(0.25)	25	20 000	0.82(0.03)	23.76(1.32)
12.13	5 000	0.30(0.01)	9.76(1.64)	25	25 000	1.33(0.04)	19.06(1.05)

times $\rho^{-1/3} \sqrt{k_B T/m}$. $\rho^{-1/3}$ corresponds to the interatomic spacing. $\sqrt{k_B T/m}$ corresponds to the thermal velocity of the atom. Similarly, one may define the viscosity in the FVM as

$$\eta_{\text{FVM}}(V, T) = \rho^{2/3} \sqrt{m k_B T} C_\eta \exp[v_\eta(V, T)], \quad (12)$$

where C_η is a dimensionless constant and v_η is the normalized activation volume for viscosity. We assume that the exponents Q_D , Q_η , v_D , and v_η follow the functional form $(a_0 + a_1 f + a_2 f^2)t^\alpha$ with $f \equiv V_0/V$ and $t \equiv T/T_0$ ($V_0 = 6.97 \text{ \AA}^3/\text{atom}$ and $T_0 = 10\,000 \text{ K}$). The coefficients a_0 , a_1 , a_2 , and α are determined by fitting the AIMD results and listed in Tables II and III. As shown in Fig. 3, both the Arrhenius model and the free volume model fit the data well, with fitting errors 0.20×10^{-8} and $0.23 \times 10^{-8} \text{ m}^2/\text{s}$ for D , 0.53 and 0.47 mPa s for η . The main advantage of the free volume model, however, is that it reveals an inherent connection between D and η . As shown in Fig. 4, except for the difference in sign, $v_D(V, T)$ and $v_\eta(V, T)$ are very similar. In fact, one could simply assume that $v_D(V, T) = -v_\eta(V, T)$ and fit D and η simultaneously. The

TABLE II. Arrhenius model parameters for D [Eq. (9)] and η [Eq. (10)].

	D_0 (m ² /s) or η_0 (Pa s)	a_0	a_1	a_2	α
D	3.844×10^{-7}	-0.136	-4.273	0.776	-0.465
η	0.208×10^{-3}	-1.444	3.384	-0.264	-0.418

resulting fitting errors are comparable to those of v_D and v_η fitted independently: 0.23×10^{-8} vs $0.18 \times 10^{-8} \text{ m}^2/\text{s}$ for D and 0.47 vs 0.46 mPa s for η . We, therefore, prefer the free volume model with $v_D(V, T) = -v_\eta(V, T)$ to describe transport properties of liquid iron as it is simpler. Moreover, it uncovers the connection between D and η , which otherwise would be unnoticed.

A natural consequence of $v_D(V, T) = -v_\eta(V, T)$ is that the product of D and η satisfies the Stokes–Einstein relation,⁵¹

$$\frac{D\eta}{\rho^{1/3} k_B T} = \text{const.} \quad (13)$$

This relation has been found to be valid under the pressure–temperature conditions of the Earth’s outer core.^{10,15,20} Here, we show that it holds to even higher P – T conditions corresponding to the cores of massive exoplanets.

To compare our results with prior studies,^{11,15,46,49,52} we convert above $D(V, T)$ and $\eta(V, T)$ into $D(P, T)$ and $\eta(P, T)$ using the thermal equation of state of liquid iron. The results are shown in Fig. 5. Good agreement validates our approach and lends supports to our

TABLE III. Free volume model parameters for D [Eq. (11)] and η [Eq. (12)].

	C_D or C_η	a_0	a_1	a_2	α
D	0.347	-0.755	2.764	-0.168	-0.678
η	0.313	0.755	-2.764	0.168	-0.678

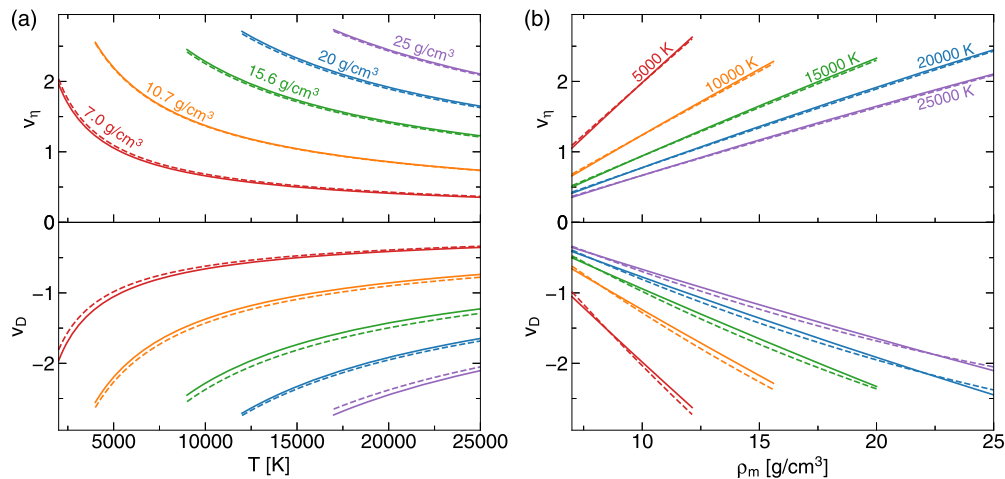


FIG. 4. Normalized activation volumes in the free volume model as functions of (a) temperature and (b) density. The solid (dashed) lines represent simultaneous (independent) fittings of D and η , respectively.

predictions at even higher pressures and temperatures, which are yet to be systematically studied.

C. Atomic excess entropy scaling

Atomic transport properties under different P - T conditions are related by the atomic excess entropy scaling law. To check the validity of this law, we first rescale the length and time in the units of $\rho^{-1/3}$ and $\rho^{-1/3}\sqrt{m/k_B T}$. The self-diffusion coefficient and viscosity then become

$$D^* = \rho^{1/3} (m/k_B T)^{1/2} D, \quad (14)$$

$$\eta^* = \rho^{-2/3} (m k_B T)^{-1/2} \eta. \quad (15)$$

We then calculate the exact atomic excess entropy by

$$S_{\text{ex}} \equiv S - S_{\text{ele}} - S_{\text{ig}}, \quad (16)$$

where S is the total entropy of the system, S_{ele} is the electronic entropy, and S_{ig} is the entropy of the ideal atomic gas. We apply a recently developed thermodynamic integration (TI) approach²¹ to determine the total entropy S . At $\rho_m = 7.0 \text{ g/cm}^3$ and 1800 K, our calculated entropy is $12.13 k_B/\text{atom}$, in excellent agreement with the experimental value ($12 k_B/\text{atom}$).⁵³ S_{ele} and S_{ig} are determined from the standard entropy formula for the free electron gas and the ideal atomic gas, respectively. The results are shown in Fig. 6. Note that S_{ex} does not follow the same temperature dependence as the total entropy S : S_{ex} rises slowly at high temperatures, resembling a hard sphere gas whose S_{ex} is temperature independent. By contrast, the total entropy S depends on T more strongly due to its S_{el} and S_{ig} components. This feature will have interesting consequences when considering transport properties along geophysically important thermal profiles.

The atomic excess entropy scaling law states that D^* and η^* are explicit functions of S_{ex} only. Density and temperature will not

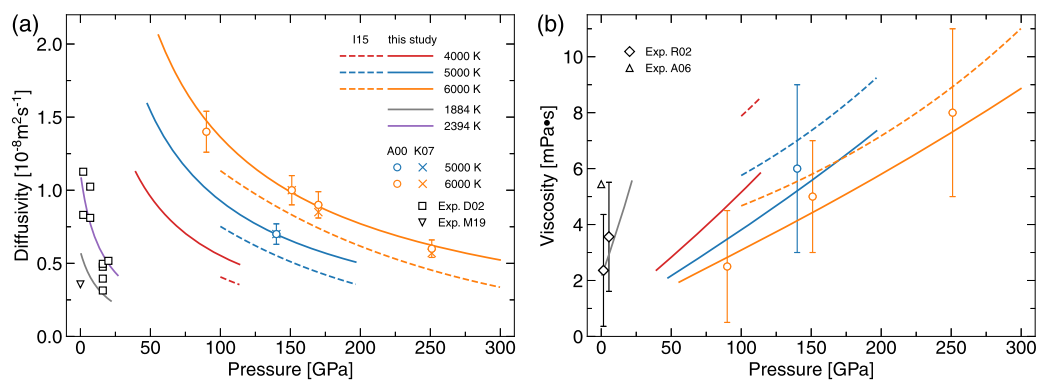


FIG. 5. Comparisons of (a) diffusivity and (b) viscosity at low pressures with experiments (D02,⁴⁶ M19,⁴⁷ R02,⁴⁸ and A06⁴⁹) and other theoretical calculations (A00,¹¹ K07,¹³ and I15¹⁵).

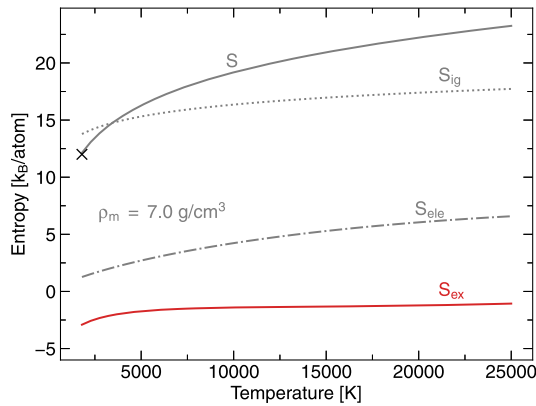


FIG. 6. Various entropy components of liquid iron at $\rho_m = 7.0 \text{ g/cm}^3$. The excess entropy S_{ex} does not follow the same temperature dependence as the total entropy S .

play direct roles. We find that, indeed, this is the case up to 25 g/cm^3 and $25\,000 \text{ K}$. As shown in Fig. 7, $D^* = 0.621 \exp(0.842S_{\text{ex}})$ and $\eta^* = 0.171 \exp(-0.843S_{\text{ex}})$, respectively. These expressions are very close to the quasi-universal scaling law found by Rosenfeld¹⁸ for strongly coupled fluids, with $D^* \approx 0.6 \exp(0.8S_{\text{ex}})$ and $\eta^* \approx 0.2 \exp(-0.8S_{\text{ex}})$. By contrast, Cao *et al.*²⁰ found $D^* \approx 0.383 \exp(0.707S_{\text{ex}})$ and $\eta^* = 0.412 \exp(-0.688S_{\text{ex}})$. Cao *et al.*²⁰ conducted simulations with classical molecular dynamics and used the pair correlation entropy S_2 to approximate S_{ex} , both of which may contribute to the discrepancy. In principle, the relation established by AIMD and exact S_{ex} should be more realistic.

The aforementioned results were obtained with non-spin-polarized AIMD simulations, yet liquid iron is paramagnetic at low pressures and temperatures.^{54–56} It is therefore important to understand how atomic transport properties of liquid iron may be affected by magnetism. To this end, we ran a collinear spin-polarized^{57,58} AIMD simulation at 7.0 g/cm^3 and 1800 K . Following the work of Desjarlais,⁵⁹ we applied the two-phase thermodynamic model with a memory function correction (2pt-mf) to evaluate the ionic entropy S_{ion} and then determined S_{ex} as $S_{\text{ion}} - S_{\text{ig}}$. Tests on the non-spin-polarized case indicate that the entropy predicted by the 2pt-mf method is accurate within 1% ($0.1k_B/\text{atom}$). To get the total entropy S_{tot} for the spin-polarized case, we also included the magnetic entropy $S_{\text{mag}} = k_B(1 + \langle \delta m_s^2 \rangle^{1/2})$, where $\langle \delta m_s^2 \rangle^{1/2}$ is the standard deviation of the local magnetic moment evaluated over all iron

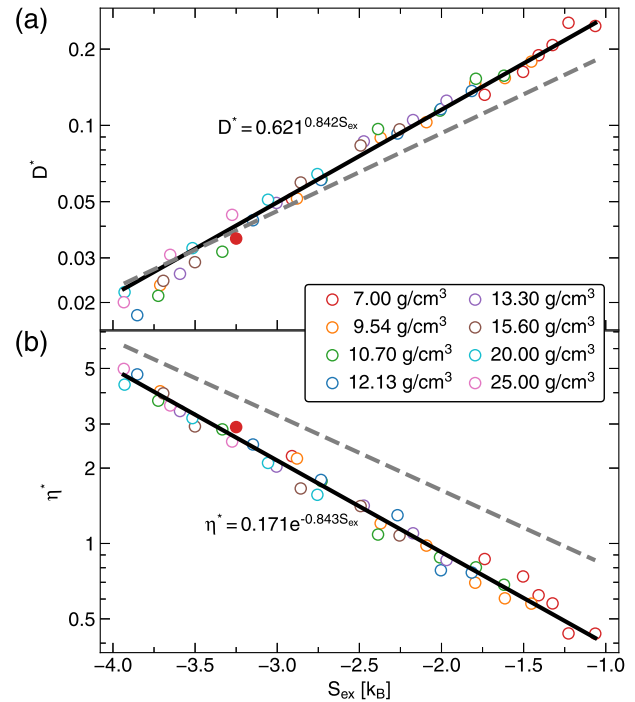


FIG. 7. (a) Reduced diffusivity D^* and (b) viscosity η^* of liquid iron as functions of the excess entropy S_{ex} . The vertical axis is plotted on a logarithmic scale. The open circles represent the non-spin-polarized AIMD results, which are fitted by the solid lines. The closed circles represent spin-polarized AIMD results at 7.0 g/cm^3 , 1800 K . Apparently, they follow the same atomic excess entropy scaling law as the non-spin-polarized results. The dashed lines represent the scaling law found by Cao *et al.*²⁰ where $D^* = 0.383 \exp(0.707S_{\text{ex}})$ and $\eta^* = 0.412 \exp(-0.688S_{\text{ex}})$. The results of the present study satisfy the quasi-universal scaling law found by Rosenfeld¹⁸ for strongly coupled fluids where $D^* \approx 0.6 \exp(0.8S_{\text{ex}})$ and $\eta^* \approx 0.2 \exp(-0.8S_{\text{ex}})$.

atoms and AIMD steps. The results are summarized in Table IV. The diffusivity predicted by spin-polarized AIMD is $0.44 \times 10^{-8} \text{ m}^2/\text{s}$, $\sim 43\%$ lower than the value from non-spin-polarized simulation. The viscosity from spin-polarized AIMD is 2.95 mPa s , $\sim 35\%$ higher. While such variations are notable, they are within the differences among experimental measurements. Korell *et al.*⁵⁵ calculated the electronic transport properties of liquid iron using collinear spin-polarized and non-spin-polarized simulations. Near the

TABLE IV. Thermal properties of liquid iron at 7.0 g/cm^3 and 1800 K predicted by non-spin-polarized (“non-spin”) and spin-polarized (“spin”) AIMD simulations. “Expt.” denotes experimental data at the ambient melting point (7.019 g/cm^3 , 1811 K).

	P (GPa)	$S_{\text{ele}}(k_B)$	$S_{\text{ion}}(k_B)$	$S_{\text{mag}}(k_B)$	$S_{\text{tot}}(k_B)$	$S_{\text{ex}}(k_B)$	$D(10^{-8} \text{ m}^2/\text{s})$	η (mPa s)
Non-spin	-16.7(3)	1.22(1)	10.91(4)		12.13(5)	-2.91(4)	0.63(4)	1.92(16)
Spin	-3.9(3)	0.70(1)	10.51(4) ^a	1.02(1)	12.23(5)	-3.27(4)	0.44(2)	2.95(28)
Expt.					12.0 ⁵³		0.83 ⁴⁶	2.36 ⁴⁸
							0.28 ⁴⁷	5.44 ⁴⁹

^a2pt-mf.

ambient melting point, the electrical conductivity determined from spin-polarized simulations is $\sim 20\%$ lower than non-spin-polarized simulations. Here, we see that atomic transport properties are affected by magnetism to a similar extent. More interestingly, even though D and η predicted by spin-polarized and non-spin-polarized simulations differ in value, they follow the same atomic excess entropy scaling law as the differences in D and η get compensated by the change in S_{ex} . This indicates that liquid planetary iron cores may share the same form of atomic excess entropy scaling law, regardless of their magnetic status.

A comparison between Eqs. (14) and (15) and Eqs. (11) and (12) reveals that the excess entropy scaling law and the free volume model are closely related. Indeed, D^* equals $C_D \exp[v_D(V, T)]$ and η^* equals $C_\eta \exp[v_\eta(V, T)]$. The $v_D = -v_\eta$ relation identified in Sec. III B is not a coincidence, but a consequence of the fact that D^* and η^* satisfy the atomic excess entropy scaling law.

IV. DISCUSSION

With $D(\rho, T)$ and $\eta(\rho, T)$ determined in Sec. III, we now examine the diffusivity and viscosity along the iron melting curve. There are two temperature profiles requiring careful consideration: one is the iron melting curve. For a planet possessing a solid inner core and a liquid outer core, its transport properties near the inner-core boundary (ICB) would correspond to those of iron near the melting curve; the other is the isentropic line, which corresponds to the temperature profile of a liquid core under active convection. For Earth, the pressure associated with the isentropic line starts from 136 GPa at the core-mantle boundary (CMB) to 330 GPa at the ICB. For other planets, the relevant pressures differ substantially from tens of GPa for planets such as Mercury and Mars^{2,4} to a few TPa for massive exoplanets.¹⁶ Here, we consider from the ambient pressure to 2.5 TPa so as to establish how atomic transport properties of planetary cores may be affected by varying P - T conditions.

Figure 8 summarizes transport properties along the iron melting curve, determined by Bouchet *et al.*⁶⁰ as $T_m = 1811(P/31.3 + 1)^{1/1.99}$, where T_m is given in Kelvin and P is given in GPa. We see that D decreases rapidly at low pressures from $0.52 \times 10^{-8} \text{ m}^2 \text{ s}^{-1}$ at 0 GPa to $0.45 \times 10^{-8} \text{ m}^2 \text{ s}^{-1}$ at 40 GPa. It then starts to increase slowly, reaching $0.61 \times 10^{-8} \text{ m}^2 \text{ s}^{-1}$ at 2.5 TPa. By contrast, η increases rapidly when $P < 40$ GPa. At higher pressures, it continues to increase although at a much slower rate. The change in the pressure dependence indicates that one cannot simply extrapolate experimental data obtained at low pressures to high pressures. Such extrapolations may lead to substantial overestimation of η .⁶¹

The observed pressure dependence can be understood from the atomic excess entropy scaling law. As shown in Fig. 8(a), the atomic excess entropy S_{ex} drops sharply from the ambient pressure to 150 GPa, and it then becomes nearly pressure independent along the melting line. Accordingly, D^* (η^*) decreases (increases) rapidly at low pressures and then becomes constant, as shown in Fig. 8(c). Since D and η are related to D^* and η^* as

$$D = \frac{D^*}{\rho^{1/3}(m/k_B T)^{1/2}}, \quad (17)$$

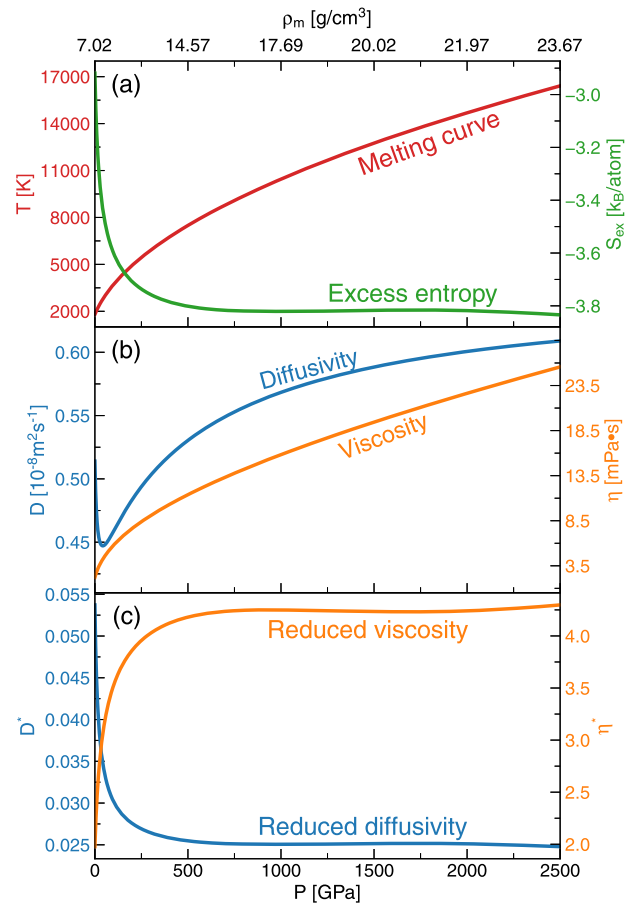


FIG. 8. Atomic transport properties along the iron melting curve. (a) Melting temperature⁶⁰ and atomic excess entropy. (b) Diffusivity and viscosity. (c) Reduced diffusivity and viscosity.

$$\eta = \frac{\eta^*}{\rho^{-2/3}(m k_B T)^{-1/2}}, \quad (18)$$

the rapid drop (rise) in D (η) at low P is mainly caused by the drop in S_{ex} . Above 150 GPa, S_{ex} remains constant; thus, D and η are controlled solely by their respective normalization factors. Recall that the melting curve can be approximated by Lindemann's law as⁶²

$$T_m = T_0 \left(\frac{\rho}{\rho_0} \right)^{2(\gamma-1/3)}, \quad (19)$$

where T_0 is the melting temperature at density ρ_0 and γ is the thermal Grüneisen parameter: one finds that $D \propto T_m^{\frac{3\gamma+1}{2(3\gamma-1)}}$ when D^* is constant. Similarly, $\eta \propto T_m^{\frac{3\gamma+1}{2(3\gamma-1)}}$ when η^* is constant. Since γ of liquid iron is above one, both D and η increase along the melting curve even when D^* and η^* remain constant. As the exponent associated with η is greater than that of D , the relative increase in η is larger. Indeed, from 150 GPa to 2.5 TPa, η increases by more than a factor of two, whereas D increases by 20%.

We now consider D and η along the isentropic line. Following the work of Anderson and Ahrens,⁶³ we start with the ambient melting point (1811 K, 0 GPa) and then integrate according to the concurrent adiabatic slope $(\partial T/\partial P)_s$. Choosing a different starting point with higher temperatures will not change the overall trends.

Figure 9(a) shows the resulting isentropic line, with D and η shown in Fig. 9(b). We see that D decreases along the isentropic line, whereas η increases. Unlike the melting curve case where D exhibits non-monotonic behavior, here, both D and η vary monotonically. Nevertheless, the changes are rapid at low P yet become sluggish at high P , which again excludes simple extrapolations.

Such pressure dependences can also be explained from the atomic excess entropy scaling law. Interestingly, while the total entropy is constant along the isentropic line, the excess entropy decreases. Accordingly, D and η are controlled by the joint effects of D^* , η^* , and their respective normalization factors. Recall that the isentropic line is related to the Grüneisen parameter γ as⁶³

$$T_s = T_0 \left(\frac{\rho}{\rho_0} \right)^\gamma, \quad (20)$$

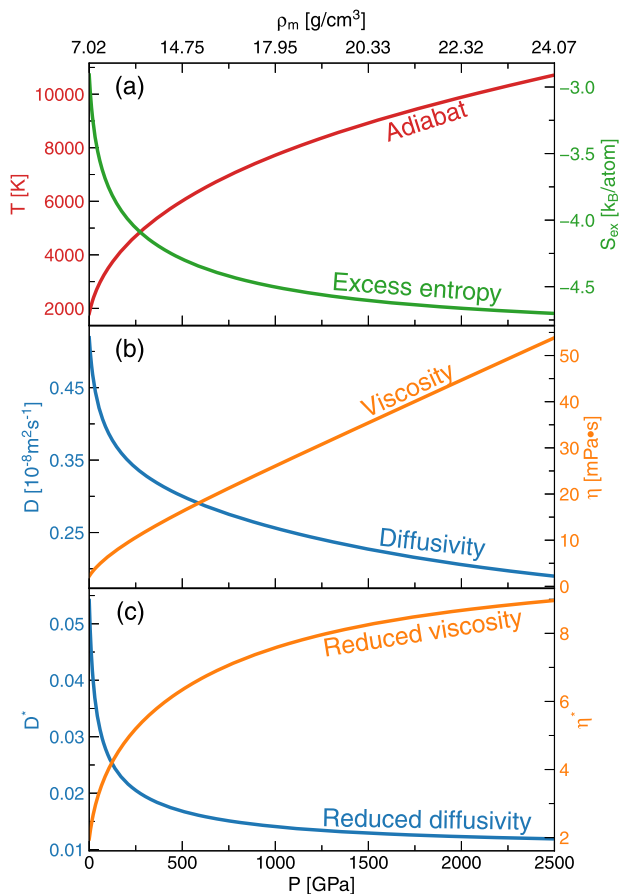


FIG. 9. Atomic transport properties along the iron isentropic line anchored at the ambient melting point (0 GPa, 1811 K). (a) Temperature profile and excess entropy. (b) Diffusivity and viscosity. (c) Reduced diffusivity and viscosity.

and we have $D \propto D^* T_s^{\frac{1}{2} - \frac{1}{3\gamma}}$ and $\eta \propto \eta^* T_s^{\frac{1}{2} + \frac{2}{3\gamma}}$. Since γ of liquid iron is above one, D^* and the associated normalization factor $T_s^{\frac{1}{2} - \frac{1}{3\gamma}}$ vary in opposite directions along the isentropic line, yet the effect of normalization factor is weaker and the temperature dependence of D is predominated by that of D^* . As D^* decreases along the isentropic line, so does D . By contrast, both η^* and its normalization factor $T_s^{\frac{1}{2} + \frac{2}{3\gamma}}$ increase along the isentropic line, causing η to increase even faster. The eventual outcome is that the relative increase in η along the isentropic line is much greater than that of D . From 0 GPa to 2.5 TPa, η increases by more than one order of magnitude, whereas D decreases by merely 50%.

From the above analysis, we see that atomic transport properties are subject to competing effects of pressure and temperature. Increasing pressure tends to hamper diffusion and causes a rise in viscosity, whereas increasing temperature has an opposite effect. Overall, liquid cores of massive exoplanets may have diffusivities 40%–50% lower than that of the Earth's outer core and viscosities an order of magnitude higher. While such differences are notable, they are unlikely to cause paradigm shifts in the fluid dynamics of liquid cores. Viscous forces are likely to be negligible compared to other major players such as the Coriolis force and the Lorentz force.⁴² Diffusion is sufficiently fast such that the core remains well-mixed without major stratifications.⁶⁴

Moreover, the present work shows that the atomic excess entropy scaling law is valid for liquid iron up to the TPa regime. This indicates that the system is dynamically invariant under uniform time and space rescaling.¹⁹ With the discovery of exoplanets with distinct masses and radii, there is much interest in finding scaling laws for planetary dynamos of different sizes.^{7,65} The fact that fluidic cores are dynamically invariant under time and space rescaling may provide an underlying mechanism for those more macroscopic, phenomenological scaling laws describing planetary dynamos. From this perspective, it would be interesting to investigate whether electronic transport properties, such as electrical conductivity and thermal conductivity, also satisfy some form of scaling laws. This, however, is beyond the scope of the present work and may be of interest for future studies.

V. CONCLUSION

We have calculated atomic transport properties of liquid iron from the ambient melting point up to the pressures and temperatures of massive exoplanets. We find that D and η can be fitted simultaneously using a generalized free volume model. This leads to simpler expressions than prior studies and reveals the intimate connection between D and η . In addition, we find that liquid iron satisfies the quasi-universal atomic excess entropy scaling law of strongly coupled liquids up to the TPa regime. We evaluate transport properties along geophysically important temperature profiles and find that they can be understood by the atomic excess entropy scaling law. Aside from providing useful material property data for modeling a wide range of planetary cores, the present work also bridges two renowned theories of liquids: the free volume model and the atomic excess entropy scaling law. Moreover, it indicates that the dynamics of liquid iron is scale-invariant. Assuming that other quantities involved in the dynamics of liquid planetary iron cores (not fully captured by the present simulations) do not affect our results, scale

invariance may provide an underlying mechanism for establishing macroscopic scaling laws of planetary dynamos.

SUPPLEMENTARY MATERIAL

See the [supplementary material](#) for (a) the accuracy of the PAW pseudo-potential; (b) convergences with respect to the size of the simulation cell, kinetic energy cutoff for plane wave expansion, and k-mesh sampling; and (c) comparisons of the non-spin-polarized and spin-polarized results.

ACKNOWLEDGMENTS

We thank Dario Alfè for providing us with the PAW pseudo-potential used in his prior work. Work at UCAS was supported by the Strategic Priority Research Program (B) of the Chinese Academy of Sciences (Grant No. XDB18000000) and the NSFC under Grant No. 41972044. Work at UCL was supported by STFC under Grant No. ST/T000163/1. Calculations were performed on Tianhe-2 at the National Supercomputer Center of China (NSCC) in Guangzhou.

AUTHOR DECLARATIONS

Conflict of Interest

The authors have no conflicts to disclose.

DATA AVAILABILITY

The data that support the findings of this study are available within the article.

REFERENCES

- 1 F. Birch, "Elasticity and constitution of the Earth's interior," *J. Geophys. Res.* **57**, 227–286, <https://doi.org/10.1029/jz057i002p00227> (1952).
- 2 A. J. Stewart, M. W. Schmidt, W. van Westrenen, and C. Lieske, "Mars: A new core-crystallization regime," *Science* **316**, 1323–1325 (2007).
- 3 S. C. Stähler, A. Khan, W. B. Banerdt, P. Lognonné, D. Giardini *et al.*, "Seismic detection of the martian core," *Science* **373**, 443–448 (2021).
- 4 J. L. Margot, S. J. Peale, R. F. Jurgens, M. A. Slade, and I. V. Holin, "Large longitude libration of Mercury reveals a molten core," *Science* **316**, 710–714 (2007).
- 5 B. A. Buffett, "Earth's core and the geodynamo," *Science* **288**, 2007–2012 (2000).
- 6 U. R. Christensen, "A deep dynamo generating Mercury's magnetic field," *Nature* **444**, 1056–1058 (2006).
- 7 E. Gaidos, C. P. Conrad, M. Manga, and J. Hernlund, "Thermodynamic limits on magnetodynamos in rocky exoplanets," *Astrophys. J.* **718**, 596–609 (2010).
- 8 M. Greff-Lefftz and H. Legros, "Core-mantle coupling and viscoelastic deformations," *Phys. Earth Planet. Inter.* **90**, 115–135 (1995).
- 9 F. Nimmo, "8.02—Energetics of the core," in *Treatise on Geophysics*, 2nd ed., edited by G. Schubert (Elsevier, Oxford, 2015), pp. 27–55.
- 10 D. Alfè and M. J. Gillan, "First-principles calculation of transport coefficients," *Phys. Rev. Lett.* **81**, 5161–5164 (1998).
- 11 D. Alfè, G. Kresse, and M. J. Gillan, "Structure and dynamics of liquid iron under Earth's core conditions," *Phys. Rev. B* **61**, 132–142 (2000).
- 12 L. Vočadlo, D. Alfè, M. J. Gillan, and G. D. Price, "The properties of iron under core conditions from first principles calculations," *Phys. Earth Planet. Inter.* **140**, 101–125 (2003).
- 13 L. Koči, A. B. Belonoshko, and R. Ahuja, "Molecular dynamics calculation of liquid iron properties and adiabatic temperature gradient in the Earth's outer core," *Geophys. J. Int.* **168**, 890–894 (2007).
- 14 M. Pozzo, C. Davies, D. Gubbins, and D. Alfè, "Transport properties for liquid silicon-oxygen-iron mixtures at Earth's core conditions," *Phys. Rev. B* **87**, 014110 (2013).
- 15 H. Ichikawa and T. Tsuchiya, "Atomic transport property of Fe-O liquid alloys in the Earth's outer core P, T condition," *Phys. Earth Planet. Inter.* **247**, 27–35 (2015).
- 16 C. T. Unterborn and W. R. Panero, "The pressure and temperature limits of likely rocky exoplanets," *J. Geophys. Res.: Planets* **124**, 1704–1716, <https://doi.org/10.1029/2018je005844> (2019).
- 17 Y. Rosenfeld, "Relation between the transport coefficients and the internal entropy of simple systems," *Phys. Rev. A* **15**, 2545–2549 (1977).
- 18 Y. Rosenfeld, "A quasi-universal scaling law for atomic transport in simple fluids," *J. Phys.: Condens. Matter* **11**, 5415–5427 (1999).
- 19 J. C. Dyre, "Perspective: Excess-entropy scaling," *J. Chem. Phys.* **149**, 210901 (2018).
- 20 Q.-L. Cao, P.-P. Wang, D.-H. Huang, J.-S. Yang, M.-J. Wan, and F.-H. Wang, "Transport coefficients and entropy-scaling law in liquid iron up to Earth-core pressures," *J. Chem. Phys.* **140**, 114505 (2014).
- 21 T. Sun, J. P. Brodholt, Y. Li, and L. Vočadlo, "Melting properties from ab initio free energy calculations: Iron at the Earth's inner-core boundary," *Phys. Rev. B* **98**, 224301 (2018).
- 22 Q.-L. Cao, X.-S. Kong, Y. D. Li, X. Wu, and C. S. Liu, "Revisiting scaling laws for the diffusion coefficients in simple melts based on the structural deviation from hard-sphere-like case," *Physica B* **406**, 3114–3119 (2011).
- 23 P. E. Blöchl, "Projector augmented-wave method," *Phys. Rev. B* **50**, 17953–17979 (1994).
- 24 G. Kresse and D. Joubert, "From ultrasoft pseudopotentials to the projector augmented-wave method," *Phys. Rev. B* **59**, 1758–1775 (1999).
- 25 G. Kresse and J. Hafner, "Ab initio molecular-dynamics simulation of the liquid-metal-amorphous-semiconductor transition in germanium," *Phys. Rev. B* **49**, 14251–14269 (1994).
- 26 G. Kresse and J. Furthmüller, "Efficiency of ab-initio total energy calculations for metals and semiconductors using a plane-wave basis set," *Comput. Mater. Sci.* **6**, 15–50 (1996).
- 27 J. P. Perdew, K. Burke, and M. Ernzerhof, "Generalized gradient approximation made simple," *Phys. Rev. Lett.* **77**, 3865–3868 (1996).
- 28 T. Sjöstrom and S. Crockett, "Quantum molecular dynamics of warm dense iron and a five-phase equation of state," *Phys. Rev. E* **97**, 053209 (2018).
- 29 K. Hakim, A. Rivoldini, T. Van Hoolst, S. Cottenier, J. Jaeken, T. Chust, and G. Steinle-Neumann, "A new ab initio equation of state of hcp-Fe and its implication on the interior structure and mass-radius relations of rocky super-Earths," *Icarus* **313**, 61–78 (2018).
- 30 D. Alfè, G. D. Price, and M. J. Gillan, "Iron under earth's core conditions: Liquid-state thermodynamics and high-pressure melting curve from ab initio calculations," *Phys. Rev. B* **65**, 165118 (2002).
- 31 P. Giannozzi, S. Baroni, N. Bonini, M. Calandra, R. Car, C. Cavazzoni, D. Ceresoli, G. L. Chiarotti, M. Cococcioni, I. Dabo, A. Dal Corso, S. de Gironcoli, S. Fabris, G. Fratesi, R. Gebauer, U. Gerstmann, C. Gougoussi, A. Kokalj, M. Lazzeri, L. Martin-Samos, N. Marzari, F. Mauri, R. Mazzarello, S. Paolini, A. Pasquarello, L. Paulatto, C. Sbraccia, S. Scandolo, G. Sclauzero, A. P. Seitsonen, A. Smogunov, P. Umari, and R. M. Wentzcovitch, "QUANTUM ESPRESSO: A modular and open-source software project for quantum simulations of materials," *J. Phys.: Condens. Matter* **21**, 395502 (2009).
- 32 J. Deng and L. Stixrude, "Thermal conductivity of silicate liquid determined by machine learning potentials," *Geophys. Res. Lett.* **48**, e2021GL093806, <https://doi.org/10.1029/2021GL093806> (2021).
- 33 S. Nosé, "A unified formulation of the constant temperature molecular dynamics methods," *J. Chem. Phys.* **81**, 511–519 (1984).
- 34 N. D. Mermin, "Thermal properties of the inhomogeneous electron gas," *Phys. Rev.* **137**, A1441–A1443 (1965).
- 35 S.-T. Lin, M. Blanco, and W. A. Goddard III, "The two-phase model for calculating thermodynamic properties of liquids from molecular dynamics: Validation for the phase diagram of Lennard-Jones fluids," *J. Chem. Phys.* **119**, 11792–11805 (2003).

- ³⁶F. Wagle and G. Steinle-Neumann, "Liquid iron equation of state to the terapascal regime from ab initio simulations," *J. Geophys. Res.: Solid Earth* **124**, 3350–3364, <https://doi.org/10.1029/2018jb016994> (2019).
- ³⁷Q. Li, J.-W. Xian, Y.-G. Zhang, T. Sun, and L. Vočadlo, Thermal Properties of Liquid Iron at Conditions of Planetary Cores (2021).
- ³⁸M. P. Allen and D. J. Tildesley, *Computer Simulations of Liquids* (Clarendon Press, Oxford, UK, 1987).
- ³⁹T. Sun, J. Xian, H. Zhang, Z. Zhang, and Y. Zhang, "Two-phase thermodynamic model for computing entropies of liquids reanalyzed," *J. Chem. Phys.* **147**, 194505 (2017).
- ⁴⁰J.-P. Hansen and I. R. McDonald, *Theory of Simple Liquids*, 4th ed. (Academic Press, Oxford, 2013).
- ⁴¹D. A. McQuarrie, *Statistical Mechanics* (University Science Books, Sausalito, 2000), Vol. 55.
- ⁴²G. A. De Wijs, G. Kresse, L. Vočadlo, D. Dobson, D. Alfè, M. J. Gillan, and G. D. Price, "The viscosity of liquid iron at the physical conditions of the Earth's core," *Nature* **392**, 805–807 (1998).
- ⁴³G. Tarjus and D. Kivelson, "Breakdown of the Stokes-Einstein relation in supercooled liquids," *J. Chem. Phys.* **103**, 3071 (1995).
- ⁴⁴C.-H. Li, X.-J. Han, Y.-W. Luan, and J.-G. Li, "Abnormal breakdown of Stokes-Einstein relation in liquid aluminium," *Chin. Phys. B* **26**, 016102 (2017).
- ⁴⁵J. W. Xian, T. Sun, and T. Tsuchiya, "Viscoelasticity of liquid iron at conditions of the Earth's outer core," *J. Geophys. Res.: Solid Earth* **124**, 11105–11115, <https://doi.org/10.1029/2019jb017721> (2019).
- ⁴⁶D. P. Dobson, "Self-diffusion in liquid Fe at high pressure," *Phys. Earth Planet. Inter.* **130**, 271–284 (2002).
- ⁴⁷A. Meyer, L. Hennig, F. Kargl, and T. Unruh, "Iron self diffusion in liquid pure iron and iron-carbon alloys," *J. Phys.: Condens. Matter* **31**, 395401 (2019).
- ⁴⁸M. D. Rutter, R. A. Secco, H.-J. Liu, T. Uchida, M. L. Rivers, S. R. Sutton, and Y.-B. Wang, "Viscosity of liquid Fe at high pressure," *Phys. Rev. B* **66**, 060102(R) (2002).
- ⁴⁹M. J. Assael, K. Kakosimos, R. M. Banish, J. Brillo, I. Egry, R. Brooks, P. N. Quested, K. C. Mills, A. Nagashima, Y. Sato, and W. A. Wakeham, "Reference data for the density and viscosity of liquid aluminum and liquid iron," *J. Phys. Chem. Ref. Data* **35**, 285–300 (2006).
- ⁵⁰M. H. Cohen and D. Turnbull, "Molecular transport in liquids and glasses," *J. Chem. Phys.* **31**, 1164–1169 (1959).
- ⁵¹L. Costigliola, D. M. Heyes, T. B. Schröder, and J. C. Dyre, "Revisiting the Stokes-Einstein relation without a hydrodynamic diameter," *J. Chem. Phys.* **150**, 021101 (2019).
- ⁵²Y. Kono, C. Kenney-Benson, Y. Shibasaki, C. Park, G. Shen, and Y. Wang, "High-pressure viscosity of liquid Fe and FeS revisited by falling sphere viscometry using ultrafast X-ray imaging," *Phys. Earth Planet. Inter.* **241**, 57–64 (2015).
- ⁵³M. W. Chase, *NIST-JANAF Thermochemical Tables*, 4th ed. (American Institute of Physics, 1998).
- ⁵⁴Y. Waseda and K. Suzuki, "Atomic distribution and magnetic moment in liquid iron by neutron diffraction," *Phys. Status Solidi B* **39**, 669–678 (1970).
- ⁵⁵J.-A. Korell, M. French, G. Steinle-Neumann, and R. Redmer, "Paramagnetic-to-diamagnetic transition in dense liquid iron and its influence on electronic transport properties," *Phys. Rev. Lett.* **122**, 086601 (2019).
- ⁵⁶A. L. Edgington, L. Vočadlo, L. Stixrude, I. G. Wood, D. P. Dobson, and E. Holmström, "The top-down crystallisation of Mercury's core," *Earth Planet. Sci. Lett.* **528**, 115838 (2019).
- ⁵⁷U. von Barth and L. Hedin, "A local exchange-correlation potential for the spin polarized case. I," *J. Phys. C: Solid State Phys.* **5**, 1629–1642 (1972).
- ⁵⁸R. M. Martin, *Electronic Structure: Basic Theory and Practical Methods*, 2nd ed. (Cambridge University Press, Cambridge, 2020).
- ⁵⁹M. P. Desjarlais, "First-principles calculation of entropy for liquid metals," *Phys. Rev. E* **88**, 062145 (2013).
- ⁶⁰J. Bouchet, S. Mazevet, G. Morard, F. Guyot, and R. Musella, "Ab initio equation of state of iron up to 1500 GPa," *Phys. Rev. B* **87**, 094102 (2013).
- ⁶¹D. E. Smylie, V. V. Brazhkin, and A. Palmer, "Direct observations of the viscosity of Earth's outer core and extrapolation of measurements of the viscosity of liquid iron," *Phys.-Usp.* **52**, 79–92 (2009).
- ⁶²O. L. Anderson and A. Duba, "Experimental melting curve of iron revisited," *J. Geophys. Res.: Solid Earth* **102**, 22659–22669, <https://doi.org/10.1029/97jb01641> (1997).
- ⁶³W. W. Anderson and T. J. Ahrens, "An equation of state for liquid iron and implications for the Earth's core," *J. Geophys. Res.: Solid Earth* **99**, 4273–4284, <https://doi.org/10.1029/93jb03158> (1994).
- ⁶⁴J. Mound, C. Davies, S. Rost, and J. Aurnou, "Regional stratification at the top of Earth's core due to core-mantle boundary heat flux variations," *Nat. Geosci.* **12**, 575–580 (2019).
- ⁶⁵U. R. Christensen and J. Aubert, "Scaling properties of convection-driven dynamos in rotating spherical shells and application to planetary magnetic fields," *Geophys. J. Int.* **166**, 97–114 (2006).